Pretzsch *et al. Adv Struct Chem Imag* (2019) 5:5
https://doi.org/10.1186/s40679-019-0067-z

Advanced Structural and Chemical Imaging

RESEARCH Open Access

Investigation of hole-free phase plate performance in transmission electron microscopy under different operation conditions by experiments and simulations

Rebecca Pretzsch[1*], Manuel Dries[1], Simon Hettler[1], Martin Spiecker[2], Martin Obermair[1] and Dagmar Gerthsen[1]

Abstract

Hole-free phase plates (HFPPs), also known as Volta phase plates, were already demonstrated to be well suited for in-focus transmission electron microscopy imaging of organic objects. However, the underlying physical processes have not been fully understood yet. To further elucidate the imaging properties of HFPPs, phase shift measurements were carried out under different experimental conditions. Both positive and negative phase shifts occur depending on the diameter of the zero-order electron beam and the HFPP film temperature. The analysis of Thon ring patterns of an amorphous carbon test sample reveals that the phase-shifting patch can be significantly larger than the size of the zero-order beam on the HFPP film. An HFPP was used for in-focus phase contrast imaging of carbon nanotube (CNT) bundles under positive and negative phase-shifting conditions. The comparison of experimental and simulated images of CNT bundles gives detailed information on the phase shift profile, which depends on the spatial frequency in the vicinity of the zero-order beam. The shape of the phase shift profile also explains halo-like image artifacts that surround the imaged objects.

Keywords: Transmission electron microscopy, Phase contrast imaging, Phase plate, Thin film, Hole-free phase plate, Volta phase plate, Phase shift profile, Carbon nanotubes

Introduction

Organic materials are highly transparent for high-energy electrons in transmission electron microscopy (TEM), which leads to weak or even vanishing contrast in conventional in-focus TEM images. Such objects cause a negligible modulation of the amplitude of the exit wave function and only weakly influence the phase of the incoming electron wave. For a long time, defocusing of the objective lens has been commonly used to visualize the structure of weakly scattering samples by means of phase contrast [1]. However, defocusing comes along with a contrast delocalization and impedes image interpretability.

Different concepts for generating in-focus phase contrast by physical phase plates (PPs) were suggested already many years ago [2, 3]. A PP is a device installed in the back focal plane (BFP) of the objective lens, where it introduces a phase shift difference $\Delta\varphi_{PP}$ between the unscattered and the scattered electrons. In this work, we use the convention that a negative phase shift of the unscattered electrons corresponds to an advancing phase plate [4]. The transfer of the object wave by the imaging system is described by the coherent contrast transfer function (CTF), which is given by

$$\mathrm{CTF}(q) = \exp\left(-i \cdot \chi_{PP}(q)\right). \tag{1}$$

The wave aberration function

$$\chi_{PP}(q) = \pi \Delta f \lambda_e \cdot q^2 + \frac{\pi}{2} C_s \lambda_e^3 \cdot q^4 + \Delta\varphi_{PP} \tag{2}$$

*Correspondence: rebecca.pretzsch@kit.edu
[1] Laboratory for Electron Microscopy, Karlsruhe Institute of Technology (KIT), Engesserstr. 7, 76131 Karlsruhe, Germany
Full list of author information is available at the end of the article

includes phase shift contributions by the defocus Δf and the spherical aberration with the spherical aberration constant C_s as well as the phase shift $\Delta\varphi_{PP}$ of the PP. The electron wavelength is denoted by λ_e. For weak phase objects, the CTF reduces to the phase contrast transfer function (PCTF), which is proportional to $\sin\chi_{PP}$. In the power spectrum of a TEM image of a thin amorphous sample, dark and bright rings appear due to the PCTF, which are denoted as Thon rings. Without PP (i.e., $\Delta\varphi_{PP} = 0$), the wave aberration function and thus the PCTF are close to zero for low spatial frequencies. A phase shift $\Delta\varphi_{PP} = \pm\pi/2$ converts the sine-shaped PCTF into a cosine function resulting in strong phase contrast.

During the last two decades, substantial progress has been made in the experimental realization of PPs due to a general improvement in the fabrication of microstructured devices. Numerous different PP concepts have been proposed [5] with the thin-film Zernike PP being the first successful realization [6]. It consists of a thin amorphous carbon (aC) film with a small hole in the center and relies on the principle that scattered electrons passing through the film obtain an additional phase shift due to the mean inner potential of the film material. An optimal phase shift of $-\pi/2$ is achieved by adjusting the thickness of the film. Thin-film PPs are comparatively easy to fabricate, but show an ageing effect leading to charging-induced image artifacts [7]. In addition, the hole diameter determines the cut-on frequency below which phase contrast is not enhanced as scattered electrons transmitted through the hole do not gain a phase shift. Moreover, the sharp edge of the central hole causes intensity oscillations at abrupt changes of the scattering potential in the specimen, which are denoted as fringing artifacts [6, 8].

To avoid fringing, the hole-free phase plate (HFPP) was introduced recently [9, 10], with the Volta PP being the most common realization [10], and several impressive applications have been published in the recent past [11–17]. The HFPP consists of a continuous and homogeneously thin aC film without a hole and relies on the formation of a phase-shifting patch on the film induced by the high intensity of the zero-order beam (ZOB). Both positive [9] and negative [10] phase shifts have been reported. A positive phase shift can arise from positive charging due to the emission of secondary electrons from the aC film or contamination growth at the position of the ZOB [9, 18]. In the case of contamination growth, the phase shift is given by $\varphi = \sigma V_{MIP} t$ with the interaction constant σ, the mean inner potential V_{MIP}, and the local thickness t of the deposited contamination patch [19]. A negative phase shift can be explained by a change of the local work function in the region of the ZOB. With adsorbed (water) molecules acting as a dipole layer, the work function is modified if some adsorbed molecules are desorbed by the intense ZOB [20]. The induced phase shift strongly depends on ambient conditions such as the temperature of the HFPP, the electron dose, the size of the ZOB on the film, and residual gases in the vacuum [9, 10, 20, 21]. However, a clear understanding of the influence of these parameters and their control has not been achieved yet and requires further investigation.

In this work, we have analyzed the phase-shifting behavior of an HFPP by systematic phase shift measurements for different experimental conditions. Phase shift measurements were conducted for two different ZOB diameters on the HFPP film and for unheated and heated HFPPs to examine the sign and strength of the induced phase shift. The measurements show that a proper choice of the considered parameters is crucial to obtain the desired phase shift. In addition, a dependence of the phase shift on the spatial frequency q is observed. Therefore, the phase-shifting behavior of HFPPs will be described in the following by $\Delta\varphi_{PP}(q) = \varphi_{PP}(0) - \varphi_{PP}(q)$, including the q-dependence in the wave aberration function:

$$\chi_{PP}(q) = \pi\,\Delta f\,\lambda_e \cdot q^2 + \frac{\pi}{2} C_s \lambda_e^3 \cdot q^4 + \Delta\varphi_{PP}(q). \quad (3)$$

The phase shift of the unscattered electrons is denoted by $\varphi_{PP}(0)$ and we assume $\varphi_{PP}(q) \to 0$ for sufficiently high spatial frequencies q. Phase contrast imaging was conducted for a single-walled carbon nanotube (CNT) sample. Image simulations of CNT bundles are quantitatively compared with experimental HFPP images, which allows for the reconstruction of $\varphi_{PP}(q)$ at low spatial frequencies and explains halo image artifacts that surround objects in HFPP TEM images. The simulations also show that the shape of $\varphi_{PP}(q)$ at low spatial frequencies is crucial for the performance of an HFPP as a suitable phase contrast imaging tool.

Methods

HFPP implementation

The HFPP was prepared by depositing a thin aC layer by electron-beam evaporation (*PVD75*, *Kurt J. Lesker Company*, *Hastings*, *UK*) on a freshly cleaved mica sheet (*Plano*, *Wetzlar*, *Germany*, *Product No. 54*) and subsequent floating of the film on a TEM gold grid (*Plano*, *Product No. G2200A*). The film thickness was measured to be 12 nm by imaging of a cross-sectional TEM lamella that was prepared by focused ion beam milling from a simultaneously coated silicon wafer. The HFPP was mounted onto a customized HFPP holder equipped with a heating device and a temperature sensor in the vicinity of the film. The holder was attached to a Kleindiek MM3A-EM micromanipulator system (*Kleindiek*, *Reutlingen*, *Germany*) and implemented into the BFP of

a 200 kV Philips CM 200 FEG/ST transmission electron microscope (*Thermo Fisher Company, Waltham, USA*). With this setup, we achieved HFPP temperatures up to 200 °C. The experiments were carried out at an acceleration voltage of 200 kV. The spherical aberration constant of the microscope is 1.2 mm. A liquid nitrogen-cooled anticontamination device was used to improve vacuum conditions in the sample region.

During alignment, the condenser astigmatism must be well corrected to obtain a round shape of the ZOB on the HFPP film. Particular attention has to be paid to the vertical position of the HFPP film which must coincide with the BFP of the objective lens. The position of the BFP is aligned by adjusting the C2 lens current [22]. If the HFPP is not in the BFP, the granularity of the HFPP film becomes visible in the image at intermediate magnification. By varying the C2 lens current, the vertical position of the BFP is adjusted until the image of the film disappears. For each measurement, a fresh position on the HFPP film was used after performing the vertical adjustment close to the new HFPP film position.

Phase shift determination and HFPP TEM imaging

We present phase shift measurements conducted at room temperature with a small and a large condenser aperture (50 µm and 150 µm) resulting in a small (~ 100 nm) and large (~ 250 nm) diameter of the ZOB on the HFPP film and in addition at an HFPP film temperature of 200 °C with a small ZOB diameter. Time series of images were recorded with a 4 k charge-coupled device camera (*TVIPS, Gauting, Germany*). After each series, the HFPP film was imaged in defocused diffraction mode to reveal the imprint of the ZOB on the HFPP film. Since this mode is not a calibrated imaging mode, the size of the patches was subsequently measured in a scanning electron microscope.

An aC film with 50 nm thickness was used as test specimen to determine the phase shift induced by the HFPP by analyzing the power spectrum of the image intensity, which represents the square of the PCTF, being proportional to $\sin^2 \chi_{PP}$. Imaging was performed at relatively large underfocus values to obtain a sufficient number of Thon rings in the power spectrum. After background subtraction and envelope correction [23], the azimuthally averaged intensity profile is determined. The phase shift profile $\varphi_{PP}(q)$ can be extended and might cause an additional q-dependent shift of the inner Thon rings. For the outer rings (i.e., high q), where we assume that the phase shift no longer depends on q, the experimental power spectrum can be fitted by $\sin^2 \chi_{PP}$ with a constant phase shift $\Delta\varphi_{PP}(q) = \varphi_{PP}(0)$. This procedure yields the defocus Δf and $\varphi_{PP}(0)$. For the inner rings, the deviation between the measured power spectrum and the fit yields a first estimate of the phase shift profile $\varphi_{PP}(q)$. For simplicity, only minima and maxima of the measured power spectrum are evaluated in this case. The phase shift profile $\varphi_{PP}(q)$ is determined in more detail by comparison of experimental and simulated HFPP TEM images of CNT bundles, as outlined in "Comparison between experimental and simulated HFPP images".

Phase contrast images were acquired for a CNT sample. The sample was fabricated by laser evaporation of a composite carbon/nickel catalyst target (*Tōyō Tanso, Osaka, Japan*) and deposited on a holey carbon film (*Plano, Product No. S147-2*). The CNTs appear in bundles of parallel single CNTs and partially protrude into vacuum regions.

Results and discussion

The following chapter is divided into three subsections. The first subsection contains the analysis of the phase shift of HFPPs under different operation conditions. The results of HFPP TEM imaging of a CNT sample are described in the second subsection. The third subsection is devoted to the comparison of experimental and simulated image intensity profiles of CNT bundles, which yields detailed information on the phase shift profile for low spatial frequencies.

Phase shift measurements

Time series of images of the aC test specimen were acquired and the corresponding Thon ring patterns were evaluated to examine the phase-shifting behavior of HFPPs under different conditions (cases A–C, see Table 1 for an overview). For cases A (small ZOB, ~ 100 nm) and C (large ZOB, ~ 250 nm), the HFPP was kept at room temperature (25 °C). For case B (small ZOB), the HFPP temperature was raised to 200 °C. For case A, the phase shift evolution was so fast that image acquisition had to be performed in video mode of the camera at 13 kX magnification. For cases B and C, an acquisition time of 2 s at 97 kX magnification with a waiting time of 4 s between each image was used. For each case, results of a representative time series are depicted in Fig. 1, showing the evolution of the phase shift $\varphi_{PP}(0)$ of the ZOB and

Table 1 Overview of the different experimental conditions: diameter of the ZOB on the HFPP film, HFPP film temperature, and phase shift $\varphi_{PP}(0)$ after 30 s (case A) and 150 s (cases B and C)

Case A	Case B	Case C
Small ZOB (100 nm)	Small ZOB (100 nm)	Large ZOB (250 nm)
25 °C	200 °C	25 °C
3π	-0.8π	-3.5π

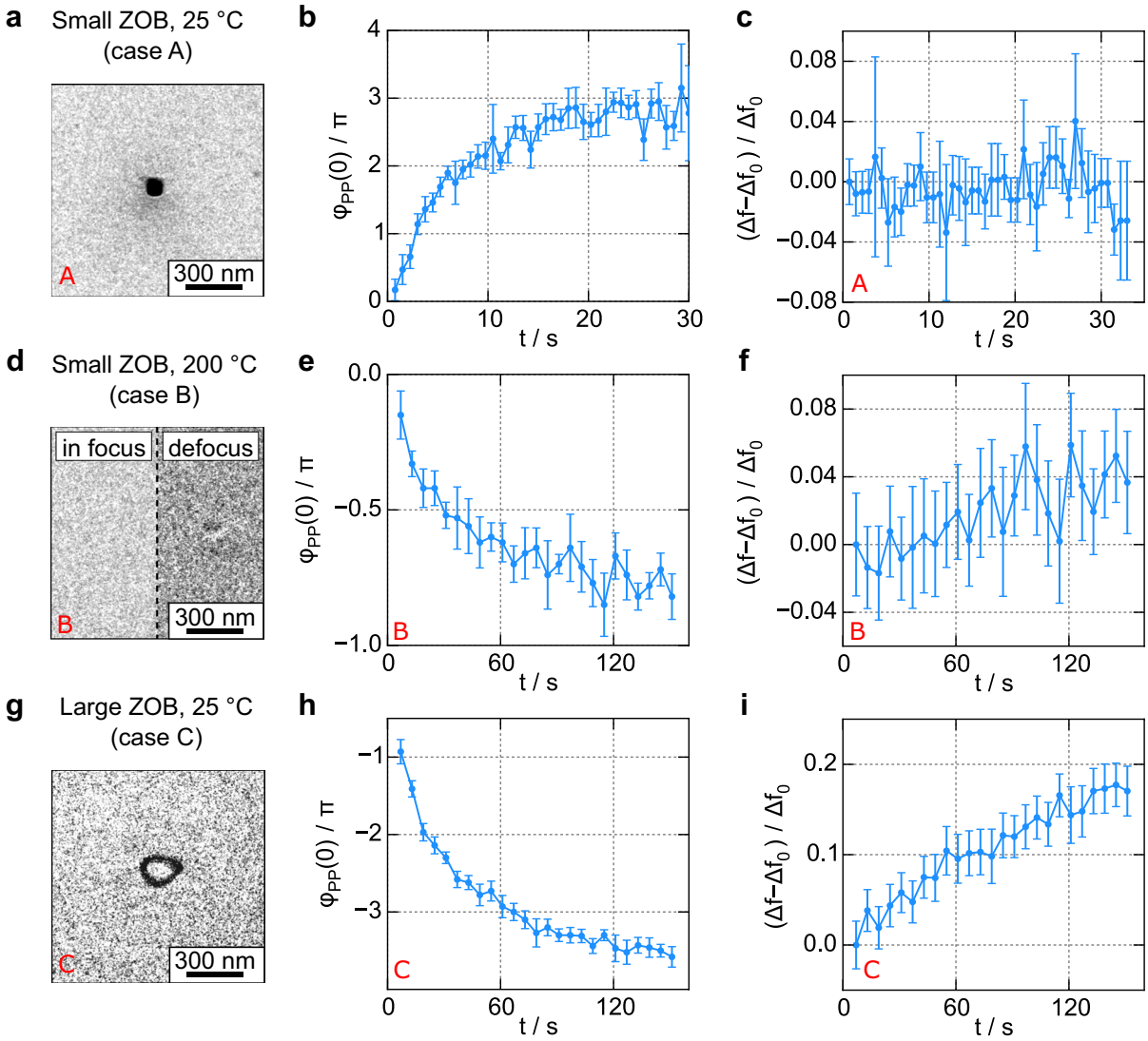

Fig. 1 TEM images of the patch on the HFPP film, phase shift evolution, and defocus change with respect to the initial defocus Δf_0 over time for cases A, B, and C. **a**–**c** Case A: small ZOB without HFPP heating. Contamination forms at the center of the ZOB. The phase shift is positive and the defocus is stable (initial value: $\Delta f_0 = -9.96$ µm). **d**–**f** Case B: small ZOB with HFPP temperature of 200 °C. No contamination is visible on the HFPP film. A defocused image of the film shows a dark shadow that originates from the irradiation by the ZOB. The phase shift is negative and amounts to about -0.8π after 2 min. The defocus changes by about 5% (initial value: $\Delta f_0 = -0.62$ µm). Note the different time scale compared to case A. **g**–**i** Case C: large ZOB without heating. Contamination forms at the rim of the ZOB. The phase shift is negative and reaches a value of -3.5π after 2–3 min. The defocus changes by about 18% (initial value: $\Delta f_0 = -1.73$ µm)

the defocus change as a function of time as well as TEM images of the ZOB imprint on the HFPP film.

For an unheated HFPP, we expect positive phase shift according to the literature [9], which can be attributed to contamination growth and the positive mean inner potential V_{MIP} of the contamination patch [18]. This is in agreement with the experimental findings for case A, where the induced phase shift is positive and builds up to $\varphi_{\mathrm{PP}}(0) = 3\pi$ within ~20 s (Fig. 1b). The dark spot on the HFPP film at the position of the ZOB indicates a strong thickness increase of the aC film by contamination (Fig. 1a). A measurement over longer time scales was not reasonable, because the signal became very weak due to strong electron scattering in the contamination patch.

For a heated HFPP with small ZOB diameter (case B), contamination is suppressed and a negative phase shift is measured as expected [10]. The phase shift evolution starts close to $\varphi_{\mathrm{PP}}(0) = 0$ and reaches $\varphi_{\mathrm{PP}}(0) = -0.8\pi$

after approximately 150 s (Fig. 1e), yielding the best phase-shifting conditions in our experiments. Contamination is not visible in the focused TEM image of the ZOB imprint (Fig. 1d). However, the dark shadow in the defocused TEM image indicates that a phase-shifting patch is formed at the position of the ZOB. It was already demonstrated that increasing temperatures lead to a reduction of the absolute value of $\varphi_{PP}(0)$ [10]. The operation temperature was limited to 200 °C in this work, which prevented further optimization of $\varphi_{PP}(0)$ towards -0.5π. The sign change of $\varphi_{PP}(0)$ indicates that a completely different mechanism is responsible for the phase shift compared to case A. Hettler et al. [20] suggested that the negative phase shift can be explained by a change of the local work function after desorption of adsorbed (water) molecules on the HFPP surface by the intense ZOB.

For the unheated HFPP with large ZOB (case C), we measured a negative phase shift with $\varphi_{PP}(0) = -3.5\pi$ after 150 s (Fig. 1h), even though contamination was present. The origin of the negative $\varphi_{PP}(0)$ can be understood by considering the TEM image of the contamination patch (Fig. 1g), which clearly differs from case A (Fig. 1a), where the ZOB was smaller. For case C, contamination only builds up at the edge of the ZOB, because weakly bound hydrocarbon molecules on the surface diffuse towards the ZOB and are deposited at its rim [24], which prevents contamination in the central region. Thus, the unscattered electrons do not experience any positive phase shift but a negative phase shift instead due to electron stimulated desorption of the water dipole layer on the film surface. Although a positive phase shift should have been imposed on electrons passing through the contamination ring, the effect was not distinct enough to be resolved in the Thon ring pattern. However, the experimental results for case C show that the effect evoking a negative phase shift can also occur at room temperature leading to even higher negative values of $\varphi_{PP}(0)$.

For an analysis of the phase shift profile, the Thon ring patterns obtained from the last image of each time series will be discussed in the following. An azimuthally averaged intensity profile of the experimental Thon ring pattern (black line) and the fitted PCTF (blue line) are shown in Fig. 2a for case A (small ZOB, unheated HFPP) after 30 s of illumination. The complete Thon ring pattern can be well fitted with $\varphi_{PP}(0) = (2.76 \pm 0.06)\pi$ and $\Delta f = (-9.63 \pm 0.12)$ µm indicating a vanishing extension of the phase-shifting patch.

Figure 2b shows the Thon ring pattern for case B (small ZOB, HFPP temperature 200 °C) after 150 s of illumination. A q-dependence of the phase shift causes an additional unknown shift of the inner Thon rings. Therefore, only spatial frequencies with $q > 1\ \mathrm{nm}^{-1}$ were considered for the fit, which yields $\varphi_{PP}(0) = (-0.82 \pm 0.05)\pi$ and $\Delta f = (-0.65 \pm 0.13)$ µm. The difference between the experimental data and the fit (cf. "Phase shift determination and HFPP TEM imaging") yields the phase shift profile $\varphi_{PP}(q)$, which is shown in the lower graph of Fig. 2b. The outer radius of the phase-shifting patch on the HFPP in the BFP is given by $r \approx 1\ \mathrm{nm}^{-1} \cdot \lambda_e \cdot L = 4$ µm (focal length $L = 1.7$ mm, $\lambda_e = 2.51$ pm), which clearly exceeds the ZOB radius of 100 nm.

A discrepancy between the PCTF fit and the experimental Thon ring pattern is also found for case C (large ZOB, no HFPP heating) after 150 s of HFPP illumination, as shown in Fig. 2c. The fit of the Thon ring pattern for $q > 1\ \mathrm{nm}^{-1}$ yields $\varphi_{PP}(0) = (-3.55 \pm 0.11)\pi$ and $\Delta f = (-1.73 \pm 0.03)$ µm. The resulting $\varphi_{PP}(q)$ is plotted in the lower graph of Fig. 2c. The measurements for case C are qualitatively equivalent to the results for case B, but the phase shift is more pronounced. This can be explained by two effects. It was suggested that the negative $\varphi_{PP}(0)$ increases with the diameter of the charged patch [20]. In addition, the concentration of adsorbed molecules should be higher at low temperature, leading to a higher work function. At this point, it is not possible to identify the dominant effect and additional measurements are required for clarification.

An indication that the φ_{PP} profile may extend to even higher q can be seen in Fig. 1f (case B) and i (case C), where the fitted defocus values increase in magnitude over time by about 5% or 18%, respectively. The variation of the fitted defocus values suggests that $\varphi_{PP}(q)$ has still not completely dropped to zero for the fitted Thon rings, which leads to an error in the determination of Δf and φ_{PP}. For a more precise determination of $\varphi_{PP}(0)$, damping by partial coherence of the electron wave at high q values could be reduced using a smaller defocus. On the other hand, this would yield a smaller number of Thon rings and thus less information on the φ_{PP} profile. Either way, the HFPP performance depends strongly on the phase shift profile at low spatial frequencies.

We add that for case A (positive phase shift), it might be possible that a negative phase shift builds up simultaneously, but is not visible in the measurement, because only the first 30 s of HFPP illumination could be analyzed. In fact, additional measurements at HFPP film temperatures of 100 °C (not shown here), where contamination builds up more slowly, showed both positive and negative phase shifts. This is in agreement with the findings from [4, 20] and indicates that contamination and negative charging can occur simultaneously.

HFPP TEM imaging of CNT bundles

Phase contrast imaging is demonstrated for negative and positive phase shifts (cases B and A) using a

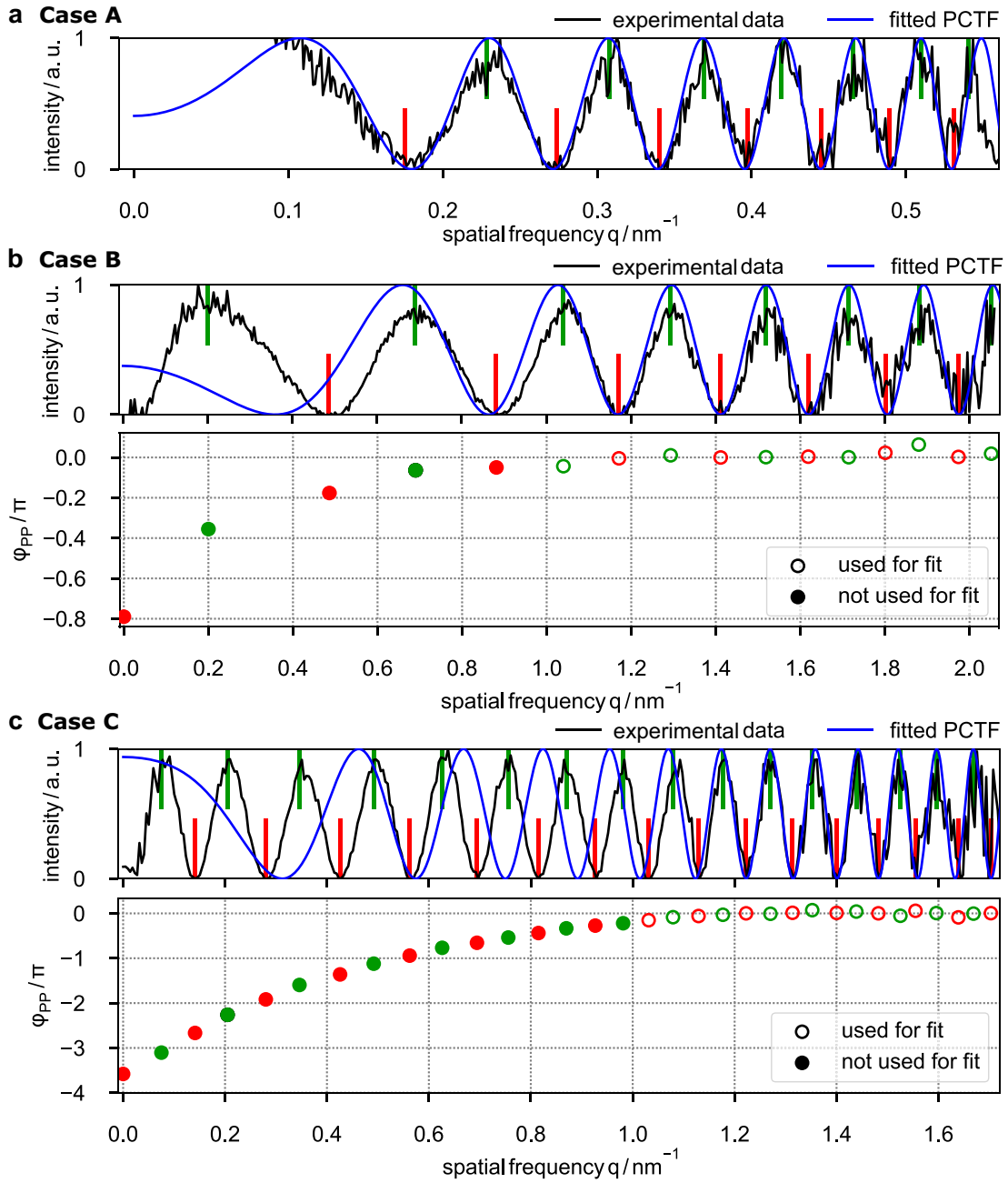

Fig. 2 Thon ring patterns of images of an amorphous carbon sample taken with an HFPP operated under case A, B, C conditions and corresponding phase shift profiles $\varphi_{PP}(q)$. **a** Case A (small ZOB diameter ~ 100 nm, unheated HFPP) with experimental Thon ring pattern and PCTF fit after 30 s of HFPP illumination. Fit parameters are $\varphi_{PP}(0) = (2.76 \pm 0.06)\pi$ and $\Delta f = (-9.63 \pm 0.12)$ µm. Minima and maxima of the experimental Thon ring pattern marked by red and green lines do not show distinct deviations between experimental data and fit. **b** Case B (small ZOB, HFPP temperature 200 °C) with experimental Thon ring pattern and PCTF fit after 150 s of illumination (upper graph) with $\varphi_{PP}(0) = (-0.82 \pm 0.05)\pi$ and $\Delta f = (-0.65 \pm 0.13)$ µm. Pronounced differences occur for minima and maxima of the experimental Thon ring pattern and the PCTF fit at small q. The extended phase shift profile $\varphi_{PP}(q)$ (lower graph) was calculated as the difference between the argument of the fitted PCTF and the experimental Thon ring pattern. **c** Case C (large ZOB ~ 250 nm, unheated HFPP) with experimental Thon ring pattern and PCTF fit (upper graph) after 150 s of illumination with $\varphi_{PP}(0) = (-3.55 \pm 0.11)\pi$ and $\Delta f = (-1.73 \pm 0.03)$ µm. Pronounced differences occur for minima and maxima of the experimental Thon ring pattern and PCTF at small q. The extended phase shift profile $\varphi_{PP}(q)$ (lower graph) was calculated as the difference between the argument of the fitted PCTF and the experimental Thon ring pattern

CNT sample. Application of the HFPP under case B conditions (small ZOB, HFPP temperature 200 °C) is illustrated in Fig. 3. Conventional bright-field TEM images of CNT bundles in focus and at an underfocus of −330 nm are shown in Fig. 3a, b. CNT bundles are barely visible in Fig. 3a as expected for phase objects. Defocusing leads to contrast enhancement and the appearance of Fresnel fringes at the bundle edges (Fig. 3b). Inserting the HFPP with $\varphi_{PP}(0) = -0.8\pi$ close to focus (Fig. 3c) strongly enhances the contrast, whereby CNT bundles and CNTs within the bundles (inset in Fig. 3c) become visible. Intensity line profiles from the same sample position (arrows in Fig. 3a–c), normalized with respect to the vacuum intensity I_0, are shown in Fig. 3d and reveal contrast enhancement of the HFPP image (red line) compared to the conventional in-focus TEM image (blue line). In contrast to a Zernike PP [6, 25], fringing artifacts due to the abrupt onset of $\Delta\varphi_{PP}(q)$ do not emerge. However, a bright halo occurs at the edge of the CNT bundles, which can be attributed to the extended phase shift profile (cf. Fig. 2) and will be verified by simulations in the next section.

Figure 4 illustrates the phase-shifting behavior under case A conditions (small ZOB, unheated HFPP). Figure 4a–c presents HFPP TEM images of CNT bundles during build-up of an increasingly positive phase shift after 2, 6, and 12 s which results from contamination growth. A smaller magnification was used here, because the fast build-up of contamination required shorter exposure times. CNT bundles and some catalyst agglomerates are clearly visible. The images show contrast reversals, which are particularly well visible for the CNT bundles in the central part of the images. The CNT contrast is reversed from bright (Fig. 4a) to dark (Fig. 4b) and bright again (Fig. 4c). Contrast reversals are also observed for the broad halos that surround the CNT bundles. Intensity line profiles across a CNT bundle (arrows in Fig. 4a–c) are shown in Fig. 4d. The complete image sequence is provided as Additional file 1. The contrast inversions in Fig. 4 are consistent with the measurement of the phase shift evolution over time (Fig. 1b). After 2, 6, and 12 s,

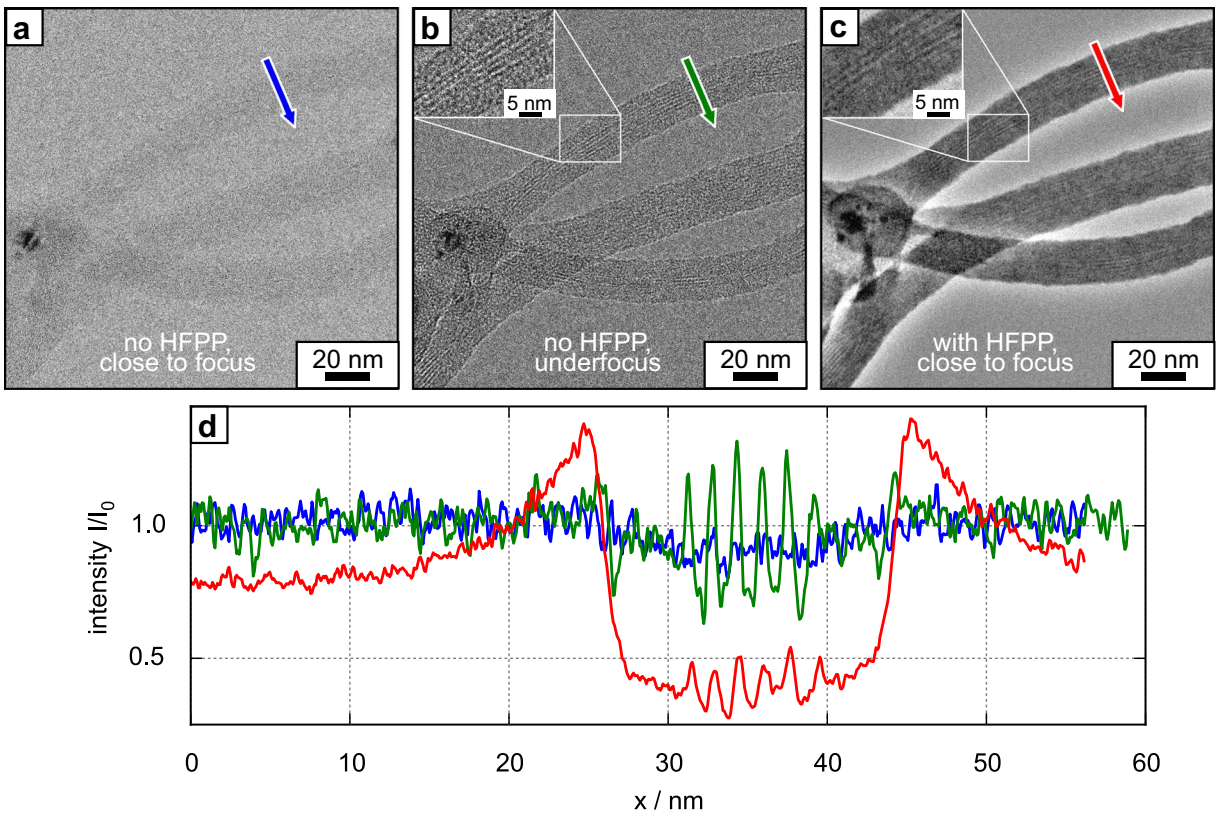

Fig. 3 TEM images of a CNT sample without HFPP and with an HFPP under case B conditions (small ZOB with HFPP temperature 200 °C, $\varphi_{PP}(0) = -0.8\pi$). **a** Conventional TEM image without HFPP close to focus. The sample is hardly visible. **b** Conventional TEM image without HFPP in underfocus conditions. CNT bundles and single CNTs become visible. **c** HFPP TEM image close to focus with significantly increased contrast. A bright halo appears around the CNT bundles. **d** Intensity line profiles along the arrows in **a**–**c**. The background signal in the HFPP image is reduced by 21% due to inelastic scattering in the HFPP film. The intensity is normalized with respect to the vacuum intensity without HFPP

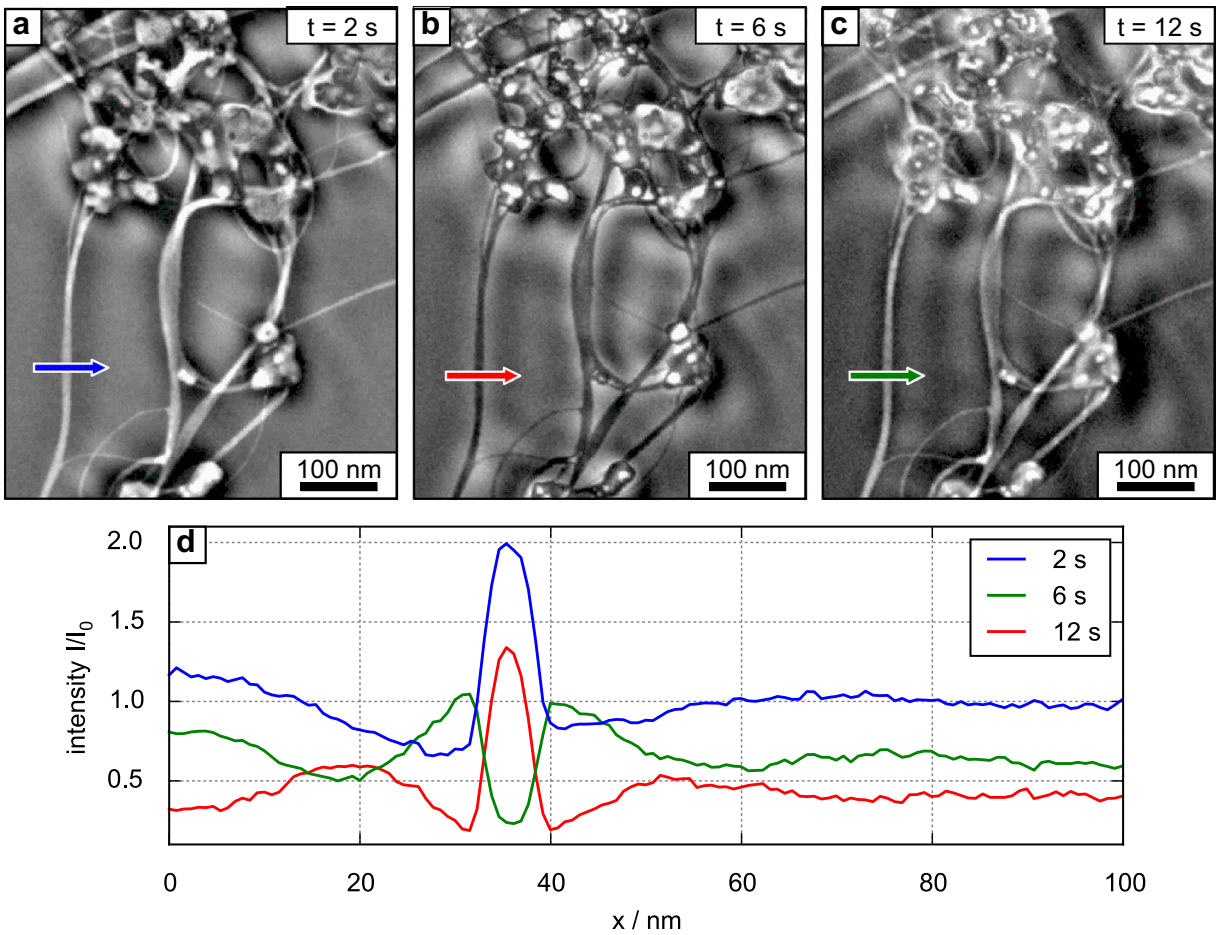

Fig. 4 TEM images of CNT bundles taken with an HFPP under case A conditions (small ZOB at room temperature). **a**–**c** Images of the same sample region after 2 s, 6 s and 12 s of illumination corresponding to phase shifts of 0.5π, 1.5π and 2.5π (cf. Fig. 1b). Due to strong contamination growth at the ZOB and the corresponding change of phase shift, contrast inversions are observed. **d** Intensity profiles along the arrows in (**a**–**c**). The signal decreases over time due to scattering in the contamination patch with increasing thickness

the phase shift is approximately $\varphi_{\mathrm{PP}}(0) = 0.5\pi$, 1.5π and 2.5π, which leads to the observed contrast inversions. After 12 s, the background signal is reduced by 60% due to the increase of electron scattering in the contamination deposited at the phase-shifting patch. Even though the small extension of the phase shift profile for positive phase shifts (see Fig. 2a) is advantageous, the strong signal decrease makes this operation mode unsuitable for phase contrast imaging as long as contamination growth cannot be controlled.

Comparison between experimental and simulated HFPP images

We simulated HFPP TEM images of CNT bundles taking into account the extended phase shift profile of the HFPP and compared simulated and experimental images. The simulations provide instructive information on the shape of $\varphi_{\mathrm{PP}}(q)$ and allow a quantitative understanding of artifacts in HFPP TEM images.

Figure 5a depicts an HFPP TEM image acquired under case B conditions, which is analyzed by simulations in this section. The black lines in Fig. 5c, e show intensity profiles across the small and the large CNT bundle in Fig. 5a. The intensity values of the small bundle are vertically shifted by 0.3 for better visualization. For the simulations, the bundles are approximated as homogeneous cylinders with radius r yielding the object exit wave function $\exp(i\phi(x))$, where $\phi(x) = 2\alpha\sqrt{r^2 - x^2}$ is the projected phase of the cylinder and α is the phase shift per unit length. The image intensity is simulated by a convolution of the exit wave and the point spread function given by the inverse Fourier transform of the CTF $e^{-i\Delta\varphi_{\mathrm{PP}}(q)}$ (cf. Eqs. 1 and 3 without influence of defocus and spherical aberration). To reconstruct the phase shift profile, the results of the Thon ring analysis for case B

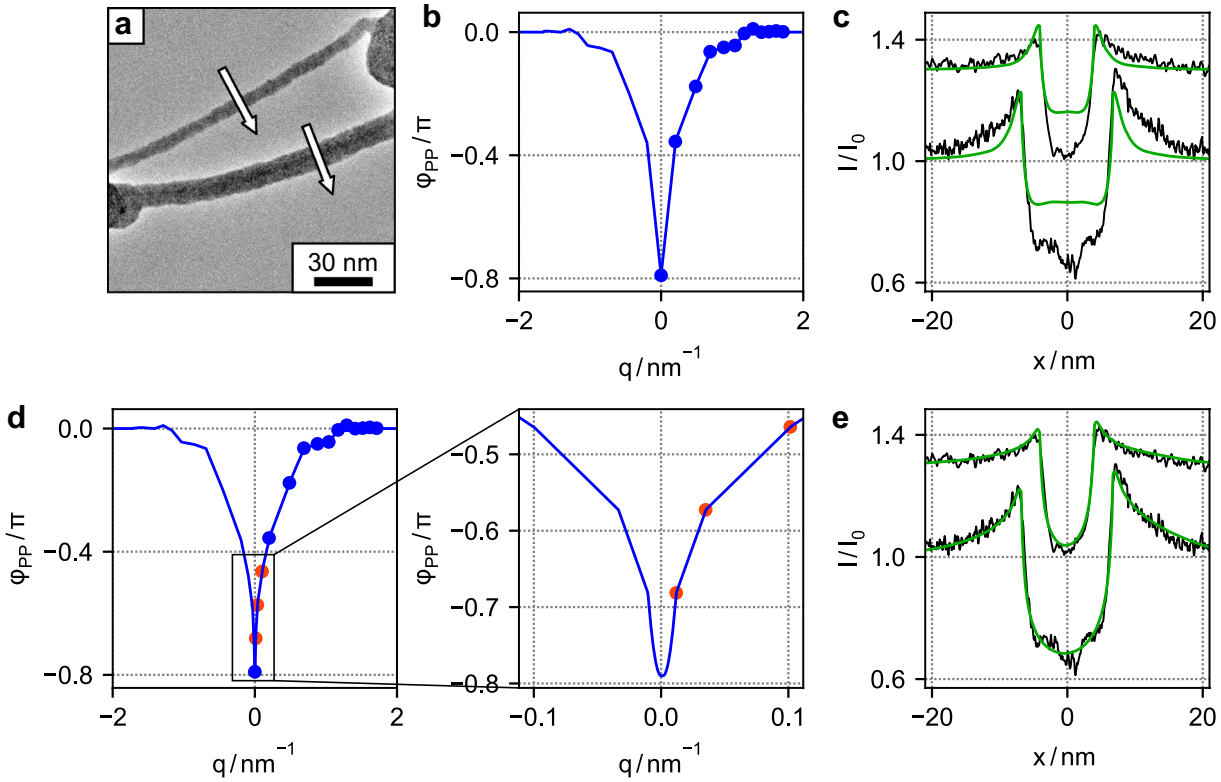

Fig. 5 Comparison of experimental and simulated image intensities of CNT bundles for an HFPP operated under case B conditions ($\varphi_{PP}(0) = -0.8\pi$). **a** HFPP TEM image showing two CNT bundles of different sizes. **b** First approximation of phase-shifting profile $\varphi_{PP}(q)$ from Fig. 2b with linear interpolation between the experimental data points (blue dots). **c** Experimental intensity line profiles (black) along the arrows in (**a**) and simulated intensity (green) for the phase shift profile shown in (**b**) do not agree well. The data for the small CNT bundle is shifted upwards by 0.3 for better visibility. **d** Phase shift profile with additional points (red) after optimization of $\varphi_{PP}(q)$ by a fit routine and zoom-in for low q. The right branch of $\varphi_{PP}(q)$ is elongated by 0.002 nm^{-1} to describe HFPP drift during exposure. **e** Experimental and simulated image intensities obtained with the phase shift profile in (**d**) are in a very good agreement. Including drift in $\varphi_{PP}(q)$ explains different halo intensities on the left and right sides of the CNT bundles

(lower graph in Fig. 2b) are used as a first approximation, because HFPP imaging and Thon ring analysis cannot be performed at the same time. Since only few data points are available for low q values, they have to be interpolated to obtain a smooth phase shift profile for the simulation. As an example, Fig. 5b shows the phase shift profile with a linear interpolation between the measured values (blue dots). The corresponding simulation (Fig. 5c) does not agree well with the experimental intensity profiles, even though a simultaneous fit of the small and the large bundle with respect to α is performed. To compensate for the lack of data points at low spatial frequencies, additional points (red dots) are added artificially between the first two blue points (Fig. 5d, e). The phase shift between the red data points is again interpolated linearly, except for the values around $q = 0$, where a parabola is used. The points are placed equidistantly along the ordinate axis, whereas their position along the abscissa is optimized by a fit routine. Furthermore, the experimental image shows asymmetric halo intensities around the CNT bundles, which can be explained by a drift of the HFPP. For this, the right branch of the phase shift profile has to be elongated by 0.002 nm^{-1}, corresponding to a drift of 8.5 nm.

Taking all these modifications into account, the resulting simulated image intensities for the small and the large CNT bundle are shown in Fig. 5e with the corresponding phase shift profile in Fig. 5d. The small elongation of the phase profile is hardly visible in the plots. The fitted value $\alpha = 0.033$ rad/nm is in reasonable agreement with the literature value for a single CNT of $\alpha \approx 0.042$ rad/nm [26] and corresponds to half of the phase shift caused by amorphous carbon, where $\alpha = C_E V_{MIP} = 0.066$ rad/nm [27]. The simulated image intensities in Fig. 5e agree well with the measured intensities for both CNT bundles. This demonstrates that the observed halo occurs due to the extended phase shift profile of the HFPP, having a sharp peak in the center with an extension similar to the size of the ZOB and long flat tails at higher spatial

frequencies, which qualitatively confirms the previous suggestions [20].

Conclusions

The phase-shifting behavior of HFPPs was studied under different operation conditions, namely, for two different ZOB diameters on the HFPP film (100 nm and 250 nm) and HFPP temperatures of 25 °C and 200 °C. A positive phase shift results from contamination at the region of the ZOB (small ZOB diameter, 25 °C). Negative phase shifts occur if contamination is prevented (small ZOB diameter, 200 °C and large ZOB, 25 °C) and are attributed to a work function change in the region of the ZOB resulting from electron-beam-induced desorption of adsorbed molecules. The amount of phase shift is suggested to depend on the thickness of the adsorbed layer and thus on the HFPP film temperature as well as on the size of the area in which the molecules are desorbed. In addition, a gradual change of the phase shift $\varphi_{\mathrm{PP}}(q)$ as a function of the spatial frequency is found for negative phase shifts, which largely exceeds the spatial frequencies that correspond to the ZOB diameter.

Strong contrast enhancement was observed for CNT bundles by in-focus HFPP TEM imaging for negative and positive φ_{PP}. The agreement of experimental and simulated image intensities of CNT bundles under negative phase-shifting conditions yields details on the shape of $\varphi_{\mathrm{PP}}(q)$. It is characterized by a sharp peak at very low q values and a flat tail extending up to $q \approx 1\ \mathrm{nm}^{-1}$, which explains the observed halo-like image artifact. The simulations show that the shape of $\varphi_{\mathrm{PP}}(q)$ at low spatial frequencies is crucial for the HFPP performance. They also demonstrate that fitting to experimental image intensities is well suited to obtain additional information on $\varphi_{\mathrm{PP}}(q)$ of an HFPP at low spatial frequencies, which cannot be accessed by Thon ring analysis. This is on one hand important for a better understanding of the underlying physics and could on the other hand be used for object wave reconstruction by a deconvolution of the image with the point spread function.

Supplementary information

Supplementary information accompanies this paper at https://doi.org/10.1186/s40679-019-0067-z.

Additional file 1: Video S1. Movie of a CNT sample acquired with an HFPP under case A operation conditions (positive phase shift) showing contrast inversions due to rapid contamination growth at the position of the intense ZOB on the HFPP film. Scale bar corresponds to 100 nm.

Abbreviations

aC: amorphous carbon; BFP: back focal plane; CNT: carbon nanotube; CTF: contrast transfer function; HFPP: hole-free phase plate; PCTF: phase contrast transfer function; PP: phase plate; TEM: transmission electron microscopy; ZOB: zero-order beam.

Acknowledgements

The authors are grateful to Patrice Brenner (Nanostructure Service Laboratory, Center for Functional Nanostructures, Karlsruhe Institute of Technology) for help with imaging the ZOB imprint in a scanning electron microscope and to Dr. Erich Müller (Laboratory for Electron Microscopy, Karlsruhe Institute of Technology) for fabrication of a TEM lamella of the HFPP film. We also thank Frank Landhäuser and Mario Nusche (Mechanical Workshop of the Physics Department, Karlsruhe Institute of Technology) for help with the construction of the HFPP heating device and Prof. Erdmann Spiecker (Friedrich-Alexander-Universität Erlangen-Nürnberg) for insightful discussions. We gratefully acknowledge funding of the project by the Deutsche Forschungsgemeinschaft (DFG) and by the Open Access Publishing Fund of the Karlsruhe Institute of Technology (KIT).

Authors' contributions

MD and DG proposed the investigation. RP and MD performed the experiments and data analysis. MO contributed to the implementation and manipulation of the PP. MS and RP implemented the simulations. SH contributed to the interpretation of the results. RP prepared the manuscript with contributions from SH, MS, MD and DG. All authors read and approved the final manuscript.

Funding

Funding was provided by the Deutsche Forschungsgemeinschaft (DFG) under Contract Number GE 841/26.

Availability of data and materials

Requests for materials should be addressed to DG (email: dagmar.gerthsen@kit.edu).

Competing interests

The authors declare that they have no competing interests.

Author details

[1] Laboratory for Electron Microscopy, Karlsruhe Institute of Technology (KIT), Engesserstr. 7, 76131 Karlsruhe, Germany. [2] Physikalisches Institut, Karlsruhe Institute of Technology (KIT), Wolfgang-Gaede-Str. 1, 76131 Karlsruhe, Germany.

Received: 9 April 2019 Accepted: 12 September 2019
Published online: 01 October 2019

References

1. Scherzer, O.: The theoretical resolution limit of the electron microscope. J. Appl. Phys. **20**(1), 20–29 (1949). https://doi.org/10.1063/1.1698233
2. Zernike, F.: Phase contrast, a new method for the microscopic observation of transparent objects. Physica **9**(7), 686–698 (1942). https://doi.org/10.1016/S0031-8914(42)80035-X
3. Boersch, H.: Über die Kontraste von Atomen im Elektronenmikroskop. Z. Naturforsch. A **2**(a), 615–633 (1947). https://doi.org/10.1515/zna-1947-11-1204
4. Malac, M., Hettler, S., Hayashida, M., Kawasaki, M., Konyuba, Y., Okura, Y., Iijima, H., Ishikawa, I., Beleggia, M.: Computer simulations analysis for determining the polarity of charge generated by high energy electron irradiation of a thin film. Micron **100**, 10–22 (2017). https://doi.org/10.1016/j.micron.2017.03.015
5. Glaeser, R.M.: Methods for imaging weak-phase objects in electron microscopy. Rev. Sci. Instrum. **84**(11), 111101 (2013). https://doi.org/10.1063/1.4830355
6. Danev, R., Nagayama, K.: Transmission electron microscopy with Zernike phase plate. Ultramicroscopy **88**(4), 243–252 (2001). https://doi.org/10.1016/S0304-3991(01)00088-2
7. Danev, R., Glaeser, R.M., Nagayama, K.: Practical factors affecting the performance of a thin-film phase plate for transmission electron microscopy. Ultramicroscopy **109**(4), 312–325 (2009). https://doi.org/10.1016/j.ultramic.2008.12.006
8. Danev, R., Nagayama, K.: Optimizing the phase shift and the cut-on periodicity of phase plates for TEM. Ultramicroscopy **111**(8), 1305–1315 (2011). https://doi.org/10.1016/j.ultramic.2011.04.004

9. Malac, M., Beleggia, M., Kawasaki, M., Li, P., Egerton, R.F.: Convenient contrast enhancement by a hole-free phase plate. Ultramicroscopy **118**, 77–89 (2012). https://doi.org/10.1016/j.ultramic.2012.02.004
10. Danev, R., Buijsse, B., Khoshouei, M., Plitzko, J.M., Baumeister, W.: Volta potential phase plate for in-focus phase contrast transmission electron microscopy. PNAS **111**(44), 15635–15640 (2014). https://doi.org/10.1073/pnas.1418377111
11. Asano, S., Fukuda, Y., Beck, F., Aufderheide, A., Förster, F., Danev, R., Baumeister, W.: A molecular census of 26*S* proteasomes in intact neurons. Science **347**(6220), 439–442 (2015). https://doi.org/10.1126/science.1261197
12. Mahamid, J., Pfeffer, S., Schaffer, M., Villa, E., Danev, R., Kuhn Cuellar, L., Förster, F., Hyman, A.A., Plitzko, J.M., Baumeister, W.: Visualizing the molecular sociology at the HeLa cell nuclear periphery. Science **351**(6276), 969–972 (2016). https://doi.org/10.1126/science.aad8857
13. Khoshouei, M., Radjainia, M., Baumeister, W., Danev, R.: Cryo-EM structure of haemoglobin at 3.2 Å determined with the Volta phase plate. Nat. Commun. **8**, 16099 (2017). https://doi.org/10.1038/ncomms16099
14. Liang, Y.L., Khoshouei, M., Radjainia, M., Zhang, Y., Glukhova, A., Tarrasch, J., Thal, D.M., Furness, S.G.B., Christopoulos, G., Coudrat, T., Danev, R., Baumeister, W., Miller, L.J., Christopoulos, A., Kobilka, B.K., Wootten, D., Skiniotis, G., Sexton, P.M.: Phase-plate cryo-EM structure of a class B GPCR-G-protein complex. Nature **546**(7656), 118–123 (2017). https://doi.org/10.1038/nature22327
15. Danev, R., Tegunov, D., Baumeister, W.: Using the Volta phase plate with defocus for cryo-EM single particle analysis. eLife **6**, e23006 (2017). https://doi.org/10.7554/elife.23006
16. Kotani, A., Harada, K., Malac, M., Salomons, M., Hayashida, M., Mori, S.: Observation of FeGe skyrmions by electron phase microscopy with hole-free phase plate. AIP Adv. **8**(5), 055216 (2018). https://doi.org/10.1063/1.5028398
17. Fukuda, Y., Laugks, U., Lučić, V., Baumeister, W., Danev, R.: Electron cryotomography of vitrified cells with a Volta phase plate. J. Struct. Biol. **190**(2), 143–154 (2015). https://doi.org/10.1016/j.jsb.2015.03.004
18. Hettler, S., Dries, M., Hermann, P., Obermair, M., Gerthsen, D., Malac, M.: Carbon contamination in scanning transmission electron microscopy and its impact on phase-plate applications. Micron **96**, 38–47 (2017). https://doi.org/10.1016/j.micron.2017.02.002
19. Willasch, D.: High resolution electron microscopy with profiled phase plates. Optik **44**, 17–36 (1975)
20. Hettler, S., Kano, E., Dries, M., Gerthsen, D., Pfaffmann, L., Bruns, M., Beleggia, M., Malac, M.: Charging of carbon thin films in scanning and phase-plate transmission electron microscopy. Ultramicroscopy **184**(A), 252–266 (2018). https://doi.org/10.1016/j.ultramic.2017.09.009
21. Hettler, S., Onoda, J., Wolkow, R., Pitters, J., Malac, M.: Charging of electron beam irradiated amorphous carbon thin films at liquid nitrogen temperature. Ultramicroscopy **196**, 161–166 (2019). https://doi.org/10.1016/j.ultramic.2018.10.010
22. Marko, M., Hsieh, C., Leith, E., Mastronarde, D., Motoki, S.: Practical experience with hole-free phase plates for cryo electron microscopy. Microsc. Microanal. **22**(6), 1316–1328 (2016). https://doi.org/10.1017/S143192761601196X
23. Barthel, J., Thust, A.: Aberration measurement in HRTEM: implementation and diagnostic use of numerical procedures for the highly precise recognition of diffractogram patterns. Ultramicroscopy **111**(1), 27–46 (2010). https://doi.org/10.1016/j.ultramic.2010.09.007
24. Hren, J.: Specimen contamination in analytical electron microscopy: sources and solutions. Ultramicroscopy **3**, 375–380 (1978). https://doi.org/10.1016/S0304-3991(78)80057-6
25. Dries, M., Obermair, M., Hettler, S., Hermann, P., Seemann, K., Seifried, F., Ulrich, S., Fischer, R., Gerthsen, D.: Oxide-free aC/Zr0.65Al0.075Cu0.275/aC phase plates for transmission electron microscopy. Ultramicroscopy **189**, 39–45 (2018). https://doi.org/10.1016/j.ultramic.2018.03.003
26. Tonomura, A.: Electron holography, 2nd edn. Springer-Verlag, Berlin (1999). https://doi.org/10.1007/978-3-540-37204-2
27. Wanner, M., Bach, D., Gerthsen, D., Werner, R., Tesche, B.: Electron holography of thin amorphous carbon films: measurement of the mean inner potential and a thickness-independent phase shift. Ultramicroscopy **106**(4–5), 341–345 (2006). https://doi.org/10.1016/j.ultramic.2005.10.004

Publisher's Note